Accepted Manuscript

Microstructural evolution of Au/TiO$_2$ nanocomposite films: The influence of Au concentration and thermal annealing

Joel Borges, Tomas Kubart, Sharath Kumar, Klaus Leifer, Marco S. Rodrigues, Nelson Duarte, Bruno Martins, Joao P. Dias, Albano Cavaleiro, Filipe Vaz

Please cite this article as: Joel Borges, Tomas Kubart, Sharath Kumar, Klaus Leifer, Marco S. Rodrigues, Nelson Duarte, Bruno Martins, Joao P. Dias, Albano Cavaleiro, Filipe Vaz, Microstructural evolution of Au/TiO$_2$ nanocomposite films: The influence of Au concentration and thermal annealing, *Thin Solid Films* (2015), doi: 10.1016/j.tsf.2015.03.024

Microstructural evolution of Au/TiO$_2$ nanocomposite films: The influence of Au concentration and thermal annealing

Joel Borges[1,2,3,*], Tomas Kubart[4], Sharath Kumar[4], Klaus Leifer[4], Marco S. Rodrigues[1,3], Nelson Duarte[1], Bruno Martins[1], Joao P. Dias[1], Albano Cavaleiro[2], Filipe Vaz[2,3]

[1] Instituto Pedro Nunes, Laboratório de Ensaios, Desgaste e Materiais, Rua Pedro Nunes, 3030-199 Coimbra, Portugal

[2] SEG-CEMUC, Mechanical Engineering Department, University of Coimbra, 3030-788 Coimbra, Portugal

[3] Centro/Departamento de Física, Universidade do Minho, Campus de Gualtar, 4710 - 057 Braga, Portugal

[4] Solid-State Electronics, Department of Engineering Sciences, Uppsala University, P.O. Box 534, Uppsala SE-751 21, Sweden

* Corresponding author: joelborges@fisica.uminho.pt, jborges@ipn.pt

1

Abstract

Nanocomposite thin films consisting of a dielectric matrix, such as titanium oxide (TiO_2), with embedded gold (Au) nanoparticles were prepared and will be analysed and discussed in detail in the present work. The evolution of morphological and structural features was studied for a wide range of Au concentrations and for annealing treatments in air, for temperatures ranging from 200 to 800 ºC. Major findings revealed that for low Au atomic concentrations (at. %), there are only traces of clustering, and just for relatively high annealing temperatures, $T \geq 500$ ºC. Furthermore, the number of Au nanoparticles is extremely low, even for the highest annealing temperature, $T = 800$ ºC. It is noteworthy that the TiO_2 matrix also crystallizes in the anatase phase for annealing temperatures above 300 ºC. For intermediate Au contents (5 at.% $\leq C_{Au} \leq$ 15 at.%), the formation of gold nanoclusters was much more evident, beginning at lower annealing temperatures ($T \geq 200$ ºC) with sizes ranging from 2 to 25 nm as the temperature increased. A change in the matrix crystallization from anatase to rutile was also observed in this intermediate range of compositions. For the highest Au concentrations (> 20 at.%), the films tended to form relatively larger clusters, with sizes above 20 nm (for $T \geq 400$ ºC). It is demonstrated that the structural and morphological characteristics of the films are strongly affected by the annealing temperature, as well as by the particular amounts, size and distribution of the Au nanoparticles dispersed in the TiO_2 matrix.

Keywords: Magnetron Sputtering; post-deposition thermal annealing; nanocomposite films, gold nanoparticles; titanium oxide.

1. Introduction

The intense scattering and absorption of light by noble metal nanoparticles (NPs) and their sensitivity and dependence on the chemical and electromagnetic environments has been widely accepted to be of high scientific and technological interests, since these effects are not commonly observed in the responses of the correspondent bulk metals [1] [2].the strong absorption band in the visible region of the electromagnetic spectrum of some noble metals (e.g. gold or silver) is the result of some changes in the so-called localized surface plasmon resonance (LSPR) [1]. Localised surface plasmons, LSPs, are charge density oscillations, confined to metallic nanoparticles/nanostructures. In contrast to Surface Plasmons, SPs, which are longitudinal charge density oscillations that propagate along the surface of a conductor, LSPs do not propagate, and they can be used for some specific areas of scientific and/or technological interest [1].

The two most studied plasmonic metals are gold (Au) and silver (Ag) [3-9]. The first has the advantage of being chemically inert, whereas the second is preferable for some particular applications, since the damping of the SPs or LSPs is smaller than that of gold. Due to their unique properties, Au and Ag nanoparticles are often found in plasmonic metal-dielectric nanocomposites, randomly dispersed in several distinct dielectric matrices, which can vary from the very common TiO_2 to more application-driven such as those of SiO_2, Al_2O_3, etc [10, 11].

Among the various technological applications, the examples in the fields of photovoltaics [12-19], pollutant-degradation materials [20], metamaterials [21], gas sensors [22, 23] and those of surface-enhanced raman spectroscopy [24] are of particular importance, associated with several other types of possibilities within optical and sensor devices [25-28]. Moreover, the interactions of noble metal clusters, dispersed in a dielectric matrix, with biological agents may result in changes of the

3

electrical/optical levels, which give interesting possibilities for bio-sensing applications [28-34].

Most of the mentioned applications rely on the tailoring of the LSPR absorption by the noble NPs, which, in a first approach, is highly dependent on the possibility of the metallic atoms form a network of clusters at the nanometric scale [2, 6]. Another important aspect of noble NPs, when dispersed in a dielectric matrix, is that their optical response strongly depends on their clustering tendency, namely the clusters size, shape and distribution [3, 35, 36], the interaction between them [7, 37], but also on the host matrix dielectric function itself [11, 38-41].

The present work puts the main focus on the basic analysis of the influence of Au concentration and in-air thermal annealing on the structure and morphology of Au:TiO$_2$ nanocomposite thin films. Since changes in size, shape and distribution of Au clusters are fundamental parameters for tailoring of the LSPR effect [1-3, 36], a set of films with a wide range of Au concentration was prepared. The films were deposited by direct current (DC) magnetron sputtering, and in order to promote the clustering of the Au nanoparticles, the as-deposited samples were subjected to an in-air annealing protocol.

2. Experimental details

The different Au:TiO$_2$ thin films were prepared by reactive DC magnetron sputtering in a custom-made deposition system [42], using a titanium target (200×100×6 mm^3, 99.8% purity) containing various amounts of Au disks (or "pellets") placed symmetrically in the preferred erosion zone (hereafter referred as a Ti-Au target). The number of Au pellets (1 mm thick) used in each deposition varied between 1 and 10, each one with typical dimensions of ~9 mm^2 or ~18 mm^2. Therefore, it was possible to increase the Au exposed area in the Ti target, and thus enhance the flux of Au atoms

towards the substrate in order to obtain different noble metal concentrations in the as-deposited films. The power supply was set to operate in the current regulating mode, using a constant current density of 100 A.m^{-2} on the Ti-Au target. The films were prepared using a gas atmosphere composed of Ar (constant flow of 60 sccm) and O$_2$ (constant flow of 7 sccm, and a partial pressure of 5.6×10^{-2} Pa), corresponding to a total pressure of about 4.5×10^{-1} Pa. The O$_2$ flow was chosen according to the hysteresis experiment: the discharge was ignited in pure argon, at a given pressure, introducing a certain argon flow to the vacuum chamber (60 sccm). Keeping the discharge current constant, the oxygen flow was stepwise increased (after reaching a steady state). When the target was completely poisoned, the process was reversed and thus the O$_2$ flow was stepwise decreased, until the discharge was again in a pure Ar atmosphere. These results are presented in a discharge voltage *vs.* O$_2$ flow plot, as it can be observed in Fig. 1. According to these results, the target was totally poisoned for an O$_2$ flow of about 7 sccm, meaning that the partial pressure of this gas in the chamber should be enough to produce stoichiometric TiO$_2$ in the substrate.

The films were deposited onto Si substrates with (100) orientation and placed in a grounded rotating substrate holder (9 r.p.m.), heated at 100 ºC. Before each deposition, the substrates were ultrasonically cleaned and then subjected to an in-situ etching process in pure Ar atmosphere (with a gas flow of 60 sccm), applying a pulsed DC current of 0.5 A (T$_{on}$= 1536 ns and f = 200 kHz) during 1200 s. After the deposition of the complete series of films (with different amounts of Au), an in-air annealing process was carried out in order to tailor the structural and morphological features of the prepared sets of samples. The selected annealing temperatures were in the range of 200 to 800 ºC. The heating ramp used was 5 ºC/min. and the isothermal period was fixed to

1 h. The samples were let to cool down freely and then removed from the furnace, after it reached the room temperature.

The chemical composition of the films was estimated by energy-dispersive X-ray spectroscopy, using a JEOL JSM-5310/Oxford X-Max. The structural analysis of the coatings were carried out using grazing incidence X-Ray Diffraction (XRD), using a Philips X-Pert diffractometer (Co-Kα radiation), operating at an angle θ = 2º. The scans were done between 15º and 80º, with a scan step of 0.025º and an acquisition time of 1 s. By using the Winfit software [43], the XRD patterns were deconvoluted, assuming Pearson-VII functions in order to obtain the peak position and intensity, the preferential growth of the crystalline phases and to calculate the grain size from the integral breadth method. The morphological features were probed by scanning electron microscopy (SEM), using a Zeiss Merlin instrument, equipped with a field emission gun and charge compensator. Both in-lens secondary electron and energy selective backscattered electron detectors were employed. The thickness of the samples was estimated by cross-section SEM analysis and the growth rate was calculated by the ratio between the average thickness and the deposition time (90 min. for all samples).

Cross sectional samples for transmission electron microscopy (TEM) analysis were prepared by conventional sample preparation method, finishing with a grazing incidence ion bombardment in a precision ion polishing system (Gatan 691) at 5 kV at a grazing angle of 6°, followed by 3 kV at 4°. TEM and Scanning TEM (STEM) analyses of the samples were carried out on a FEI Tecnai F30 TEM equipped with a field emission source operating at an accelerating voltage of 300 kV. Conventional TEM bright field images and STEM (Z-contrast) images were taken in different regions of the film in order to obtain the average particle size and the particle size distribution of Au in TiO_2 matrix. ImageJ and Digital Micrograph software were used for particle size analysis.

6

3. Results and Discussion

3.1 Target Potential and deposition rate

The evolution of the target potential and growth rate of the as-deposited films, as a function of the Au pellets area, is plotted in Fig. 2. According to the results obtained, there seems to be a clear indication that the target potential is nearly independent of the Au pellets area, since it was always very close to 470 V. On the other hand, the growth rate of the as-deposited films showed an increase by a factor of 2 when the Au pellets area changed from 9 mm^2 to approximately 100 mm^2, varying from 4.5 to 9.5 nm.min^{-1}, respectively.

In order to explain the target behaviour one has to keep in mind that the flow of O_2 used during the film's deposition is sufficient to maintain the target totally poisoned with a superficial oxide layer, as it can be drawn by the evolution of the hysteresis curve, Fig. 1. The increase of the target potential from 320 V, in the clean target situation, towards ~470 V, can be explained by the decrease of the effective emission coefficient of the Ti target [44]. This target potential value, obtained for a discharge without any Au pellet, remains approximately constant for Au pellets areas up to ~120 mm^2. This means that the fraction of Au placed at the surface of the target is not enough to disturb significantly the plasma. In fact, taking into account the total area of the target, the maximum fraction of Au used was less than 1 % of its total surface area. Nevertheless, while the amount of Ti atoms arriving to the substrate is assumed to be nearly the same, the number of Au atoms sputtered from the compound target is significantly enhanced as the pellets area was increased. This is due to the much higher sputtering yield of gold than of titanium oxide [44]. This fact can thus explain the gradual increase of the deposition (growth) rate of the films.

3.2 Composition

The atomic concentration (at. %) of Au in the films is represented in Fig. 3 as a function of the Au pellets area. The first important note is that the increase of the Au pellets area resulted in an expected almost linear increase of the composition. The elemental concentration analysis also revealed that the atomic ratio C_O/C_{Ti} was always very close to 2 in all samples, which suggests the formation of a close-stoichiometric TiO_2 matrix. The pellets area was gradually increased from 0 to ~120 mm^2 in each deposition, which allowed obtaining atomic concentrations of Au up to 25 at.%.

A closer look to the plotted results reveals that for pellets areas between 9 and 18 mm^2, the obtained Au concentration (C_{Au}) was very close to 2 at.%. This part of the set will be named hereafter as belonging to a low Au content zone. When the Au pellets area was increased from about 30 to 70 mm^2 the films revealed atomic concentrations ranging from 5 to 15 at.%, which will be noted as an intermediate Au contents region. Increasing the area of gold further in the Ti target (~100 to 120 mm^2), the prepared films revealed Au atomic concentrations between 20 and 25 at.% of Au. This last group of 2 samples will be referred hereafter as within a high Au content region. These distinct regions are emphasized in Fig. 3.

3.3 Structural and morphological analysis

The XRD analysis of the films (see figures that follow), revealed a quasi-amorphous structure for all as-deposited samples. This is also consistent with the formation of an amorphous TiO_2 matrix, which is an expected result due to the low mobility conditions used to prepare the as-deposited samples: low substrate temperature and grounded conditions during deposition [45, 46].

In order to promote some structural and morphological changes that will be required to tailor the LSPR effect, the films were thermally annealed in air, at temperatures ranging from 200 ℃ up to 800 ℃. The thermal annealing favours the diffusion of the gold atoms throughout the oxide matrix and thus the possible formation of Au nanoparticles and clusters with different sizes and distributions, which will favour some important changes in the optical responses, as already demonstrated for annealing in vacuum atmospheres [2, 12].

The XRD patterns of representative Au concentrations as a function of the annealing temperature (displayed in the figures that follow), along with representative SEM cross-section images of the films, show a progressive crystallization of the films as the annealing temperature was increased. As expected, the crystallization of gold occurs in its typical face centred cubic (fcc) structure [ICDD card No. 04-0784]. Furthermore, one can also observe the titanium oxide (TiO_2) matrix crystallization in the anatase (a-TiO_2) form [ICDD card No. 73-1764] and, in some cases, in the rutile (r-TiO_2) form [ICDD card No. 88-1172] [45]. A detailed analysis of the three groups of samples will be carried out in the following sub-chapters.

3.3.1 Low Au content

The set of films with low Au concentrations, about 2 at.%, started to crystallize at an annealing temperature of 300 ℃, according to the results displayed in Fig. 4(b). For lower temperatures, the films exhibited broad and low intensity XRD patterns, consistent with amorphous-type structures. Regarding the oxide matrix, the diffraction patterns observed for T ≥ 300 ℃ correspond mainly to reflections in planes indexed to the anatase phase of TiO_2, a-TiO_2, labelled in Fig. 4(b). This crystalline phase persists

up to 800 ºC and the corresponding diffraction patterns are narrow and relatively intense.

Although the Au content in the films is relatively low (~ 2 at.%), one can observe some broad and low intensity XRD peaks for annealing temperatures between 500 and 800 ºC. From the analysis of Fig. 4(b), it is most likely that the gold might be crystallizing in its common face centred cubic phase [ICDD card No. 04-0784], as demonstrated by the diffraction peak at ~44.6º, indexed to the (111) plane in that structure. However, this diffraction peak is somewhat difficult to characterize due to the a-TiO$_2$ diffraction peaks present in its vicinity. There are also two other peaks, centred at 2θ positions of 52.3º and 76.8º, corresponding to diffractions in the (200) planes and (220) of gold from the same structure. The broad XRD peaks of Au seem to become more intense and narrower, which might be an indication of increasing Au nanoclusters formation.

The SEM characterisation of the group of films with low Au content is displayed in Figs. 4(a) for different annealing temperatures. The as-deposited films revealed a dense columnar-like growth [47] but, as the annealing temperature was increased, the morphology seems to have become more porous and the columns are increasingly difficult to distinguish. This is more evident in the case of the films annealed at 700 ºC and 800ºC, where the columns are replaced by grain-like regions. The SEM images of the samples annealed at 500 ºC and 700 ºC show also some bright spots, suggesting the existence of gold nanoparticles, consistent with the XRD results. The progressive growth of the Au nanoparticles with the annealing experiments results from diffusion and coalescence phenomena [48, 49], promoted by the thermal energy [12].

3.3.2 Intermediate Au content

When the gold concentration increases, the as-deposited samples maintained the columnar morphology, Fig. 5(a-i), and the XRD patterns are again broad, and with relatively low intensities. This means that the as-deposited films are also quasi-amorphous, although the concentration of Au is now higher (close to 6 at.%).

According to the XRD results for the sample with a Au concentration $C_{Au} = 6$ at.%, Fig. 5(b), one can report that the crystallization of gold in these films seems to start at lower temperatures. It also revealed an early broad peak centred at $2\theta = 44.6°$, for an annealing temperature of 200 ºC. This peak corresponds to diffraction in the (111) planes of the Au fcc structure. Moreover, the initial broad Au (111) peak becomes sharper and narrower as the annealing temperature rises. It is also evident from Fig. 5(b) the appearance of two other Au diffraction peaks, namely the (200) at 400 ºC, and the (220) at 500 ºC, which become more intense with the increase of the annealing temperature. The enhancement of the intensity of the peaks is led by the growth of gold nanoparticles, as demonstrated by the SEM images displayed in Figs. 5(a). The obtained results indicate that for the samples indexed to this intermediate Au contents group, lower temperatures are sufficient to begin the clustering process, due to higher Au volume fractions. As suggested by the SEM micrographs of the films annealed at 500 ºC, Fig. 5(a-iii), and 700 ºC, Fig. 5(a-iv), the increase of the annealing temperatures induced the formation of larger gold nanoparticles. This process is also followed by the crystallization of the amorphous oxide matrix into a-TiO$_2$, starting at a temperature of 400 ºC, Fig. 5(b), which is higher than the value found for lower Au contents (300 ºC), Fig. 4(b).

The most intense and representative diffraction peak indexed to the a-TiO$_2$ occurs at $2\theta = 29.7°$, which is consistent with the (101) planes of such crystalline structure. When present, this peak constitutes the preferential orientation of the polycrystalline a-

TiO$_2$ matrix and it is always more intense than the preferential orientation of gold, which is *fcc*-Au (111), for the films with Au concentrations up to 6 at. %. Nevertheless, as soon as the concentration of Au increased to higher concentrations (between 11 and 15 at.%), the presence of polycrystalline Au becomes more relevant, as the XRD diffractograms plotted in Fig. 6(b) demonstrate.

SEM analysis of the samples with intermediate gold concentrations (represented by the 11 at.% sample in Fig. 6) revealed the presence of Au NPs from annealing temperatures between 200 and 800 ºC, as demonstrated in Fig. 6(a), where the bright spots, corresponding to gold clusters, were screened. Due to their higher noble metal concentrations, it was possible to observe several gold nanoparticles randomly distributed in the TiO$_2$ matrix as the annealing temperature was increased (namely at 500 ºC), Fig. 6(a-ii). For even higher temperatures, namely 700 ºC and 800 ºC, the Au nanoparticles seem to aggregate in larger clusters, Fig. 6(a-iii). Furthermore, in this particular case, there are some morphological changes that stand out. In fact, not only the columnar-like growth is somewhat "destroyed" by the annealing, giving rise to porous microstructures, as observed in previous lower Au concentration films, but also nano-sized voids can be observed, Fig. 6(a-iii).

An important feature about the series of samples prepared with Au concentration of 11 at.% is that the XRD pattern of the as-deposited film has a very broad peak, between the angles of 30 and 40º, typical of poor crystalline (quasi-amorphous) films. This was not so evident in the samples with lower Au content. Since the SEM image of this as-deposited sample did not reveal the presence of Au clusters, a more detailed analysis was carried out by TEM, in order to understand if the Au is already aggregated in clusters.

Fig. 7 shows the HR-TEM images obtained in bright field (BF) of the as-deposited and annealed films with Au concentration of 11 at.%. An important result is the presence of some crystalline Au grains in the as-deposited sample, with sizes of a few nanometres, Fig. 7(a), which is in agreement with the broad XRD peak observed for this sample. On the other hand, the thermal annealing induces morphological changes in the films, such as the coalescence of the small atomic Au clusters into nanoparticles. As the annealing temperature increases, larger Au NPs are formed with increasing distances between them. It should be noted that at annealing temperatures of 300 ºC and above, one can find smaller Au NPs with sizes of about 2-3 nm and also larger Au NPs.

Regarding another sample from these intermediate compositions (C_{Au} = 15 at.%), whose diffractograms and SEM micrographs are displayed in Fig. 8, there are some important changes occurring. In fact, another crystalline phase of TiO_2 started to appear, the rutile phase (r-TiO_2), for annealing temperatures of 700 ºC. The phase transformation from a-TiO_2 to r-TiO_2 starts to occur at 700 ºC, but both phases seem to coexist in the films. These results diverge slightly from those discussed in other related works. According to M. Torrell *et al.*, when these type of films are annealed in vacuum, a complete phase transformation occurs at 700 ºC [12].

Another feature that must be highlighted is the formation of large and elongated Au clusters at higher annealing temperatures, as suggested by the SEM image of the film (C_{Au} = 15 at. %) annealed at 700 ºC, Fig. 8(a-iii). The Au clusters can have sizes close to 100 nm, as demonstrated in Fig. 9. In fact, the energy filtered backscattered electrons (BSE) image (Fig. 9), shows a clear contrast between the bright clusters and the dark TiO_2 matrix.

3.3.3 High Au content

The films with relatively high gold amounts (above 20 at.%) show again some important changes in the structural and morphological features, as demonstrated by Fig. 10. In this particular case (represented by a sample with C_{Au} = 24 at. %), the high concentration of gold allows its diffusion throughout the coating surface, when the annealing temperature is about 400 ºC. This means that the high intensity and narrow Au peaks, observed for temperatures between 400 and 800 ºC, are the result of the formation of clusters with hundreds of nm on the top of the TiO$_2$ matrix, as demonstrated in Fig. 10(a-ii).

3.3.4 Grain Size and texture phenomena evolution

Fig. 11 shows the results of the average size of the gold nanoparticles (grain size) in the films and the peak intensity ratio, Int. $_{(111)}$ / Σ Int. $_{(hkl)}$, as a function of the annealing temperature. The simulations of the XRD peaks were carried out for representative samples, except for the samples with gold concentrations of ~2 at. %, since the peak fitting was quite difficult to carry out with coherent and reliable results. Although the presence of gold nanoparticles was detected by SEM for annealing temperatures of 500 ºC in these films (Fig. 4), the low intensity signal of the diffraction patterns did not allow a reliable quantification of the grain size. In the other samples (C_{Au} > 2 at.%) it was taken into account for the calculation, when possible, the peaks indexed to the three different detected orientations: Au (111), (200) and (220).

The values of gold nanoparticles size are nearly independent of the gold concentration for temperatures of 200 and 300 ºC, taking into account the simulations of XRD patterns. Their values are about 2-3 nm, meaning that the particles are confined to nanometrical scales, as already demonstrated by SEM and TEM analysis of the films. For temperatures of 400 ºC and above, the size of the Au particles clearly start to follow

14

different tendencies, Fig. 11(a). While the films with intermediate Au concentrations (between 6 and 15 at.%) revealed a gradual increase of the grain size, the values obtained for the sample with high Au concentration (24 at.%) increase sharply, about one order of magnitude.

It was observed a smooth growth of the grain size with increasing temperature, from about 2-3 to 5-6 nm for a Au concentration of 6 at.%; a more important variation towards 12 nm for a Au concentration of 11 at.%; and a sharper increase up to about 26 nm in the series with 15 at.% of Au. In Fig. 11(b) it is also evident that the texture of the films is gradually changing as the annealing temperature increases, and other orientations such as (200) are becoming more frequent rather than the preferred orientation (111).

The samples with high Au concentrations revealed a sharp increase of the grain size when the annealing temperature was changed from 300 to 400 ºC, suffering a smooth increase thereafter. This tendency can be easily explained taking into consideration the SEM micrograph displayed in Fig. 10(a-ii). In this particular situation, one can observe the formation of (poli)crystals of Au on the top of the film, which can explain the higher values found for the grain size for temperatures between 400 and 800 ºC [12]. In this range of temperatures the texture of the films is almost unchanged, as can be observed in Fig. 11(b).

Fig. 12 summarizes the results discussed above namely the overall behaviour of the three major zones identified, corresponding to low, intermediate and high Au content. In this figure, the tendency to form large clusters with the increase of gold in the samples is schematically represented and shown by the TEM images for different samples annealed at 500 ºC. The grain size of the NPs is illustrated by the colour map embedded in Fig. 12. The TEM observations and the XRD peak fitting allowed to conclude that for

low Au contents one can only find traces of NPs clustering, while for intermediate and higher Au concentration, the Au clustering was clearly evident. The TEM images displayed in Fig. 12 are elucidative of this particular point. While the low Au content samples reveal only traces of its clustering, the two samples within the intermediate Au contents reveal clear and large nanoclusters, with sizes in the range of tens of nanometers.

The Au NPs clustering were only detected at relatively high temperatures (above 500 ºC) for low Au concentrations (C_{Au} = 2 at.%), while for the highest Au concentrations (C_{Au} = 6, 11, 15 and 24 at.%), the clustering phenomena occurred quite earlier, for annealing temperatures above 200 ºC. It is also noteworthy that some Au nanoclusters were also detected in intermediate Au concentrations, namely in the as-deposited samples, according to TEM analysis, Fig. 7.

The size of clusters increased between 3 to 5 times when moving from the intermediate region to the high Au contents zone, at annealing temperatures of 400 and 500 ºC. However, the clustering differences tend to be less abrupt in these two ranges of Au contents for high annealing temperatures.

Another point emphasized in the diagram of Fig. 12 is the structural change observed in the matrix. The anatase phase of the matrix (a-TiO$_2$) is present between 300 and 800 ºC for the series with low Au content (C_{Au} = 2 at.%) and between 400 and 800 ºC for C_{Au} > 2 at.%. In some cases ($C_{Au} \geq$ 15 at.%) at high temperatures (T $\geq$ 700 ºC) both anatase and rutile (r- TiO$_2$) phases coexist in the film.

4. Conclusions

In order to study the influence of gold concentration and annealing temperature on the microstructure of Au:TiO$_2$ films, a set of samples with a wide variation of the noble

16

metal (Au) concentration was prepared, using two main steps: (i) magnetron sputtering deposition using a Ti target with small pellets of Au placed on the preferred erosion zone, followed by (ii) thermal (annealing) treatment in air atmosphere.

The discharge voltage (-V) of the Ti-Au target was independent of the Au pellets area, remaining at ~470 V, while the deposition rate increased almost linearly form 4.5 to 9.5 nm.min.$^{-1}$. The Au pellets area variation allowed the production of several series of Au:TiO$_2$ films with gold concentrations up to 25 at.%.

For low gold concentrations, C$_{Au}$: ~2 at.%, the gold nanoparticles start to form at about 500 ºC. The number of particles is low for temperatures up to 800 ºC. The amorphous TiO$_2$ matrix crystallizes in its anatase phase from the temperature of 300 ºC. For intermediate gold concentration (between 5 at.% and 15 at.%) the formation of Au nanoparticles was clearly detected for annealing temperatures of 200 ºC. In this range of Au concentrations the matrix crystallizes in the anatase phase (a-TiO$_2$) for temperatures of 400 ºC and a phase transformation to rutile (r-TiO$_2$) is observed for gold concentration of about ~15 at.% at 700 ºC. The formation of Au clusters could also be observed for the as-deposited samples. Another important feature about the films with intermediate Au concentrations (6 to 15 at.%) is that the size and distribution of gold nanoparticles strongly depends on the Au concentration and annealing temperatures. While for temperatures up to 400 ºC it was possible to report the formation of small nanoparticles almost uniformly distributed throughout the matrix, for higher temperatures bigger clusters start to form, with elongated shapes, especially for Au concentrations between 11 and 15 at.%. Due to this aggregation of nanoparticles into clusters, the distance between them also tends to increase. For higher gold concentrations (> 20 at.%), and annealing temperatures of 400 ºC, gold crystals on the top of the films were observed.

A major conclusion that can be drawn from this work is that it is possible to obtain different Au:TiO$_2$ nanocomposites with different morphological features and Au volume fractions and, above all, gold nanoparticles/clusters with different sizes and thus variable distances between them. These features are key factors to tune the LSPR effects, according to any particular application that might be envisaged.

Acknowledgements

19

References

[1] E. Hutter, J.H. Fendler, Exploitation of Localized Surface Plasmon Resonance, Advanced Materials, 16 (2004) 1685-1706.

[2] M. Torrell, R. Kabir, L. Cunha, M.I. Vasilevskiy, F. Vaz, A. Cavaleiro, E. Alves, N.P. Barradas, Tuning of the surface plasmon resonance in TiO_2/Au thin films grown by magnetron sputtering: The effect of thermal annealing, Journal of Applied Physics, 109 (2011) 074310.

[3] A.J. Haes, C.L. Haynes, A.D. McFarland, G.C. Schatz, R.P. Van Duyne, S. Zou, Plasmonic Materials for Surface-Enhanced Sensing and Spectroscopy, MRS Bulletin, 30 (2005) 368-375.

[4] H. Takele, H. Greve, C. Pochstein, V. Zaporojtchenko, F. Faupel, Plasmonic properties of Ag nanoclusters in various polymer matrices, Nanotechnology, 17 (2006) 3499.

[5] K.R. Catchpole, A. Polman, Plasmonic solar cells, Opt. Express, 16 (2008) 21793-21800.

[6] M. Torrell, L. Cunha, M.R. Kabir, A. Cavaleiro, M.I. Vasilevskiy, F. Vaz, Nanoscale color control of TiO2 films with embedded Au nanoparticles, Materials Letters, 64 (2010) 2624-2626.

[7] P.K. Jain, M.A. El-Sayed, Plasmonic coupling in noble metal nanostructures, Chemical Physics Letters, 487 (2010) 153-164.

[8] E. Pedrueza, J. Sancho-Parramon, S. Bosch, J.L. Valdés, J.P. Martinez-Pastor, Plasmonic layers based on Au-nanoparticle-doped TiO_2 for optoelectronics: structural and optical properties, Nanotechnology, 24 (2013) 065202.

[9] A. Siozios, D.C. Koutsogeorgis, E. Lidorikis, G.P. Dimitrakopulos, T. Kehagias, H. Zoubos, P. Komninou, W.M. Cranton, C. Kosmidis, P. Patsalas, Optical Encoding by Plasmon-Based Patterning: Hard and Inorganic Materials Become Photosensitive, Nano Letters, 12 (2011) 259-263.

[10] H.T. Beyene, F.D. Tichelaar, M.A. Verheijen, M.C.M. Sanden, M. Creatore, Plasma-Assisted Deposition of Au/SiO2 Multi-layers as Surface Plasmon Resonance-Based Red-Colored Coatings, Plasmonics, 6 (2011) 255-260.

[11] J. Wang, W.M. Lau, Q. Li, Effects of particle size and spacing on the optical properties of gold nanocrystals in alumina, Journal of Applied Physics, 97 (2005) 1143031-1143038.

[12] M. Torrell, P. Machado, L. Cunha, N.M. Figueiredo, J.C. Oliveira, C. Louro, F. Vaz, Development of new decorative coatings based on gold nanoparticles dispersed in an amorphous TiO2 dielectric matrix, Surface and Coatings Technology, 204 (2010) 1569-1575.

[13] M. Torrell, L. Cunha, A. Cavaleiro, E. Alves, N.P. Barradas, F. Vaz, Functional and optical properties of Au:TiO2 nanocomposite films: The influence of thermal annealing, Applied Surface Science, 256 (2010) 6536-6542.

[14] S. Pillai, K.R. Catchpole, T. Trupke, M.A. Green, Surface plasmon enhanced silicon solar cells, Journal of Applied Physics, 101 (2007) 093105.

[15] D.M. Schaadt, B. Feng, E.T. Yu, Enhanced semiconductor optical absorption via surface plasmon excitation in metal nanoparticles, Applied Physics Letters, 86 (2005) 063106.

[16] H.A. Atwater, A. Polman, Plasmonics for improved photovoltaic devices, Nat. Mater., 9 (2010) 205-213.

[17] J.A. Schuller, E.S. Barnard, W.S. Cai, Y.C. Jun, J.S. White, M.L. Brongersma, Plasmonics for extreme light concentration and manipulation, Nat. Mater., 9 (2010) 193-204.

[18] D. Derkacs, S.H. Lim, P. Matheu, W. Mar, E.T. Yu, Improved performance of amorphous silicon solar cells via scattering from surface plasmon polaritons in nearby metallic nanoparticles, Applied Physics Letters, 89 (2006) 093103.

[19] G. Walters, I.P. Parkin, The incorporation of noble metal nanoparticles into host matrix thin films: synthesis, characterisation and applications, Journal of Materials Chemistry, 19 (2009) 574-590.

[20] J.-J. Wu, C.-H. Tseng, Photocatalytic properties of nc-Au/ZnO nanorod composites, Applied Catalysis B: Environmental, 66 (2006) 51-57.

[21] J. Sancho-Parramon, V. Janicki, H. Zorc, On the dielectric function tuning of random metal-dielectric nanocomposites for metamaterial applications, Opt. Express, 18 (2010) 26915-26928.

[22] R.M. Walton, D.J. Dwyer, J.W. Schwank, J.L. Gland, Gas sensing based on surface oxidation/reduction of platinum-titania thin films I. Sensing film activation and characterization, Applied Surface Science, 125 (1998) 187-198.

[23] B. Liedberg, C. Nylander, I. Lunström, Surface plasmon resonance for gas detection and biosensing, Sensors and Actuators, 4 (1983) 299-304.

[24] P. Alivisatos, The use of nanocrystals in biological detection, Nature Biotechnology, 22 (2004) 47-52.

[25] J. Preclíková, F. Trojánek, P. Němec, P. Malý, Multicolour photochromic behaviour of silver nanoparticles in titanium dioxide matrix, physica status solidi (c), 5 (2008) 3496-3498.

[26] D. Buso, M. Post, C. Cantalini, P. Mulvaney, A. Martucci, Gold Nanoparticle-Doped TiO2 Semiconductor Thin Films: Gas Sensing Properties, Advanced Functional Materials, 18 (2008) 3843-3849.

[27] J.N. Anker, W.P. Hall, O. Lyandres, N.C. Shah, J. Zhao, R.P. Van Duyne, Biosensing with plasmonic nanosensors, Nat. Mater., 7 (2008) 442-453.

[28] A. de la Escosura-Muñiz, C. Parolo, A. Merkoçi, Immunosensing using nanoparticles, Materials Today, 13 (2010) 24-34.

[29] X.D. Hoa, A.G. Kirk, M. Tabrizian, Towards integrated and sensitive surface plasmon resonance biosensors: A review of recent progress, Biosensors and Bioelectronics, 23 (2007) 151-160.

[30] G.L. Liu, Y.D. Yin, S. Kunchakarra, B. Mukherjee, D. Gerion, S.D. Jett, D.G. Bear, J.W. Gray, A.P. Alivisatos, L.P. Lee, F.Q.F. Chen, A nanoplasmonic molecular ruler for measuring nuclease activity and DNA footprinting, Nature Nanotechnology, 1 (2006) 47-52.

[31] D.A. Stuart, A.J. Haes, C.R. Yonzon, E.M. Hicks, R.P. Van Duyne, Biological applications of localised surface plasmonic phenomenae, IEE proceedings. Nanobiotechnology, 152 (2005) 13-32.

[32] K.A. Willets, R.P. Van Duyne, Localized surface plasmon resonance spectroscopy and sensing, in: Annual Review of Physical Chemistry, Annual Reviews, Palo Alto, 2007, pp. 267-297.

[33] X.W. Guo, Surface plasmon resonance based biosensor technique: A review, Journal of Biophotonics, 5 (2012) 483-501.

[34] M.D. Ooms, L. Bajin, D. Sinton, Culturing photosynthetic bacteria through surface plasmon resonance, Applied Physics Letters, 101 (2012) 253701.

[35] M.M. Alvarez, J.T. Khoury, T.G. Schaaff, M.N. Shafigullin, I. Vezmar, R.L. Whetten, Optical Absorption Spectra of Nanocrystal Gold Molecules, The Journal of Physical Chemistry B, 101 (1997) 3706-3712.

[36] Y. Xia, Y. Xiong, B. Lim, S.E. Skrabalak, Shape-Controlled Synthesis of Metal Nanocrystals: Simple Chemistry Meets Complex Physics?, Angewandte Chemie International Edition, 48 (2009) 60-103.

[37] K.H. Su, Q.H. Wei, X. Zhang, J.J. Mock, D.R. Smith, S. Schultz, Interparticle Coupling Effects on Plasmon Resonances of Nanogold Particles, Nano Letters, 3 (2003) 1087-1090.

[38] C. Noguez, Surface Plasmons on Metal Nanoparticles: The Influence of Shape and Physical Environment, The Journal of Physical Chemistry C, 111 (2007) 3806-3819.

[39] C. Novo, A.M. Funston, I. Pastoriza-Santos, L.M. Liz-Marzan, P. Mulvaney, Influence of the Medium Refractive Index on the Optical Properties of Single Gold Triangular Prisms on a Substrate, The Journal of Physical Chemistry C, 112 (2007) 3-7.

[40] S.H. Cho, S. Lee, D.Y. Ku, T.S. Lee, B. Cheong, W.M. Kim, K.S. Lee, Growth behavior and optical properties of metal-nanoparticle dispersed dielectric thin films formed by alternating sputtering, Thin Solid Films, 447–448 (2004) 68-73.

[41] M.C. Daniel, D. Astruc, Gold nanoparticles: Assembly, supramolecular chemistry, quantum-size-related properties, and applications toward biology, catalysis, and nanotechnology, Chemical Reviews, 104 (2004) 293-346.

[42] J. Borges, N. Martin, N.P. Barradas, E. Alves, D. Eyidi, M.F. Beaufort, J.P. Riviere, F. Vaz, L. Marques, Electrical properties of AlN_xO_y thin films prepared by reactive magnetron sputtering, Thin Solid Films, 520 (2012) 6709-6717.

[43] A. Ruhm, B.P. Topeverg, H. Dosch, Supermatrix approach to polarized neutron reflectivity from arbitrary spin structures, Physical Review B, 60 (1999) 16073.

[44] D. Depla, S. Mahieu, R. De Gryse, Magnetron sputter deposition: Linking discharge voltage with target properties, Thin Solid Films, 517 (2009) 2825-2839.

[45] N. Martin, C. Rousselot, D. Rondot, F. Palmino, R. Mercier, Microstructure modification of amorphous titanium oxide thin films during annealing treatment, Thin Solid Films, 300 (1997) 113-121.

[46] M.M. Hasan, A.S.M.A. Haseeb, R. Saidur, H.H. Masjuki, M. Hamdi, Influence of substrate and annealing temperatures on optical properties of RF-sputtered TiO2 thin films, Optical Materials, 32 (2010) 690-695.

[47] S. Mahieu, P. Ghekiere, D. Depla, R. De Gryse, Biaxial alignment in sputter deposited thin films, Thin Solid Films, 515 (2006) 1229-1249.

[48] A. Hörling, L. Hultman, M. Odén, J. Sjölén, L. Karlsson, Thermal stability of arc evaporated high aluminum-content $Ti_{1-x}Al_xN$ thin films, Journal of Vacuum Science & Technology A, 20 (2002) 1815-1823.

[49] I. Petrov, P.B. Barna, L. Hultman, J.E. Greene, Microstructural evolution during film growth, Journal of Vacuum Science & Technology A, 21 (2003) S117-S128.

Figure captions

Figure 1- Discharge voltage as a function of the oxygen flow during reactive sputtering of a titanium target mounted on a magnetron at constant current (100 A.m^{-2}) and constant argon pressure (0.3 Pa).

Figure 2 –Evolution of the target potential and deposition (growth) rate of the films as a function of the Au pellets area. The target potential was monitored during 1,5 h deposition and each data point corresponds to the equilibrium target potential. The growth rate was determined based on cross-sectional SEM observations and corresponds to the ratio between the thickness and deposition time (90 min.) of the film.

Figure 3 – Au concentration (at. %) of the as-deposited Au:TiO$_2$ films as a function of the Au pellets area.

Figure 4 – (a) SEM micrographs of a series of Au:TiO$_2$ films, with low Au content (C$_{Au}$: 2 at.%), annealed at different temperatures and (b) XRD diffractograms for all annealing temperatures.

Figure 5 – (a) SEM micrographs of a series of Au:TiO$_2$ films, with Au content of C$_{Au}$: 6 at.%, annealed at different temperatures and (b) XRD diffractograms for all annealing temperatures.

Figure 6 – (a) SEM micrographs of a series of Au:TiO$_2$ films, with Au content of C$_{Au}$: 11 at.%, annealed at different temperatures and (b) XRD diffractograms for all annealing temperatures.

Figure 7 – Cross-sectional HR-TEM micrographs of the (a) as-deposited sample and samples annealed at (b) 300 ℃, (c) 600 ℃ and (d) 800 ℃, with Au content of C$_{Au}$: 11 at.%.

Figure 8 – (a) SEM micrographs of a series of Au:TiO$_2$ films, with Au content of C$_{Au}$: 15 at.%, annealed at different temperatures and (b) XRD diffractograms for all annealing temperatures.
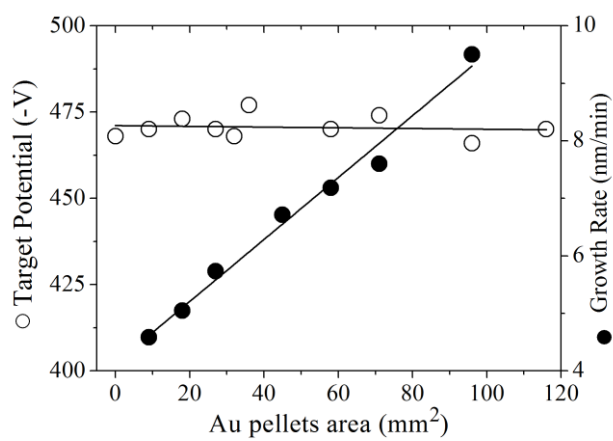
Figure 9 – SEM micrograph of the sample displayed in Fig. 8(a-iii) analyzed using the backscattered electrons (BSE) mode, providing a higher compositional contrast.

Figure 10 – (a) SEM micrographs of a series of Au:TiO$_2$ films, with high Au content (C$_{Au}$: 24 at.%), annealed at different temperatures and (b) XRD diffractograms for all annealing temperatures.

Figure 11 – Comparison of the average grain size and intensity ratio of representative samples as a function of the annealing temperature. The grain size was estimated from the integral breath method, using the Winfit software. The peaks were fitted using Pearson VI functions with a reliability of 90-95%.

Figure 12 – Diagram resuming the major results of this work. It can be observed the range of annealing temperatures where the Au NPs were detected for the different series of samples analysed; the evolution of the NPs size as a function of the temperature for different compositions; the range of temperatures where the anatase structure (*a-* TiO$_2$) is present and the range of temperatures where both anatase (*a-* TiO$_2$) and rutile (*r-* TiO$_2$) structures coexist. The HR-TEM micrographs (w×h = 85×85 nm^2) of representative samples (C$_{Au}$: 2, 11 and 15 at. %), annealed at 500 ºC, are also displayed.
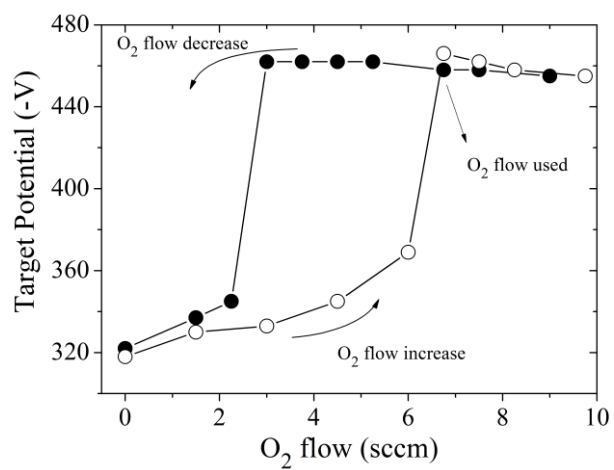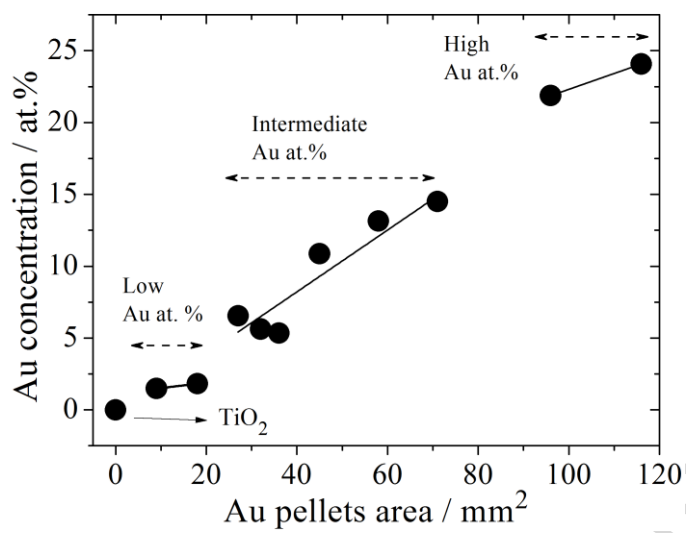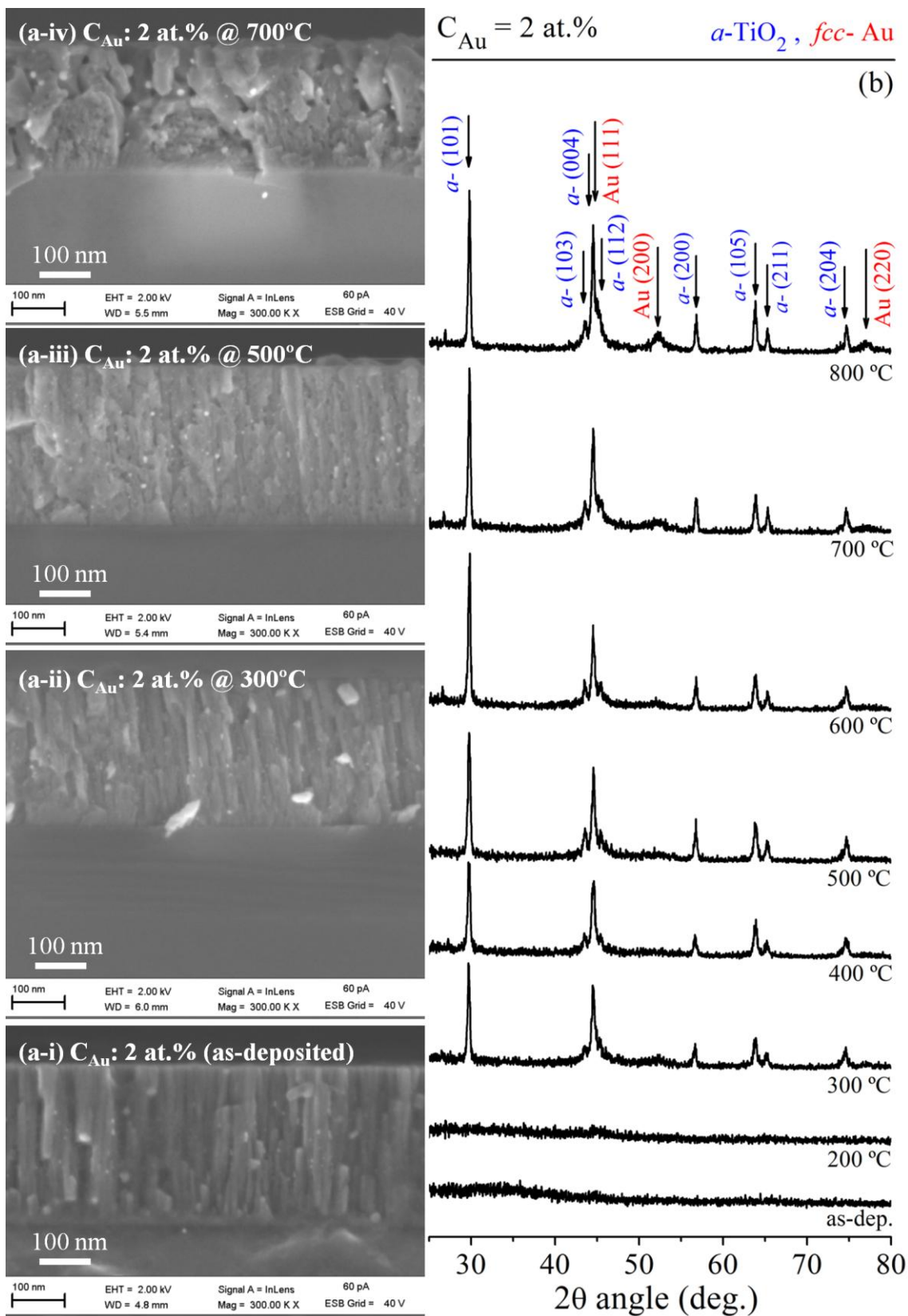
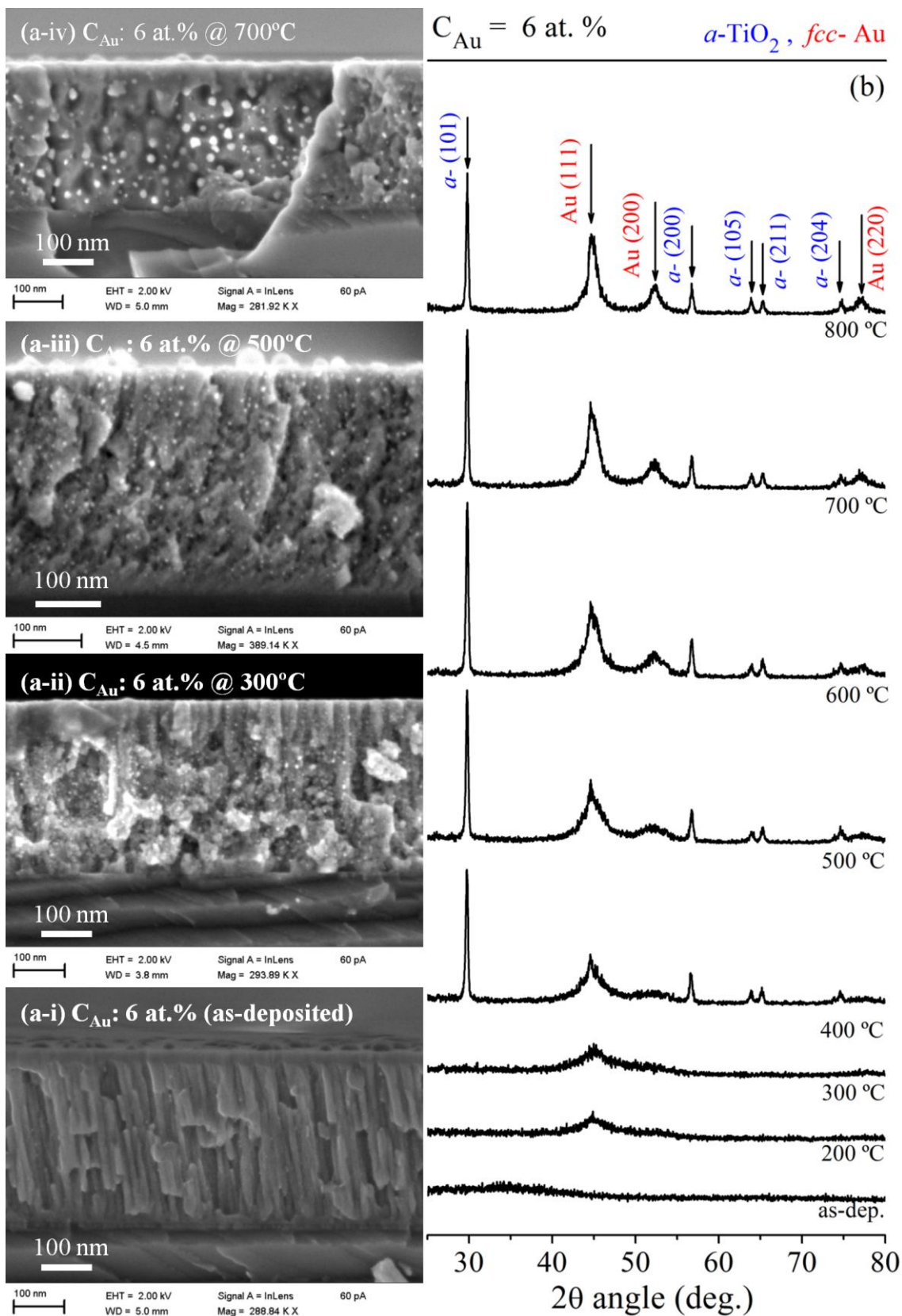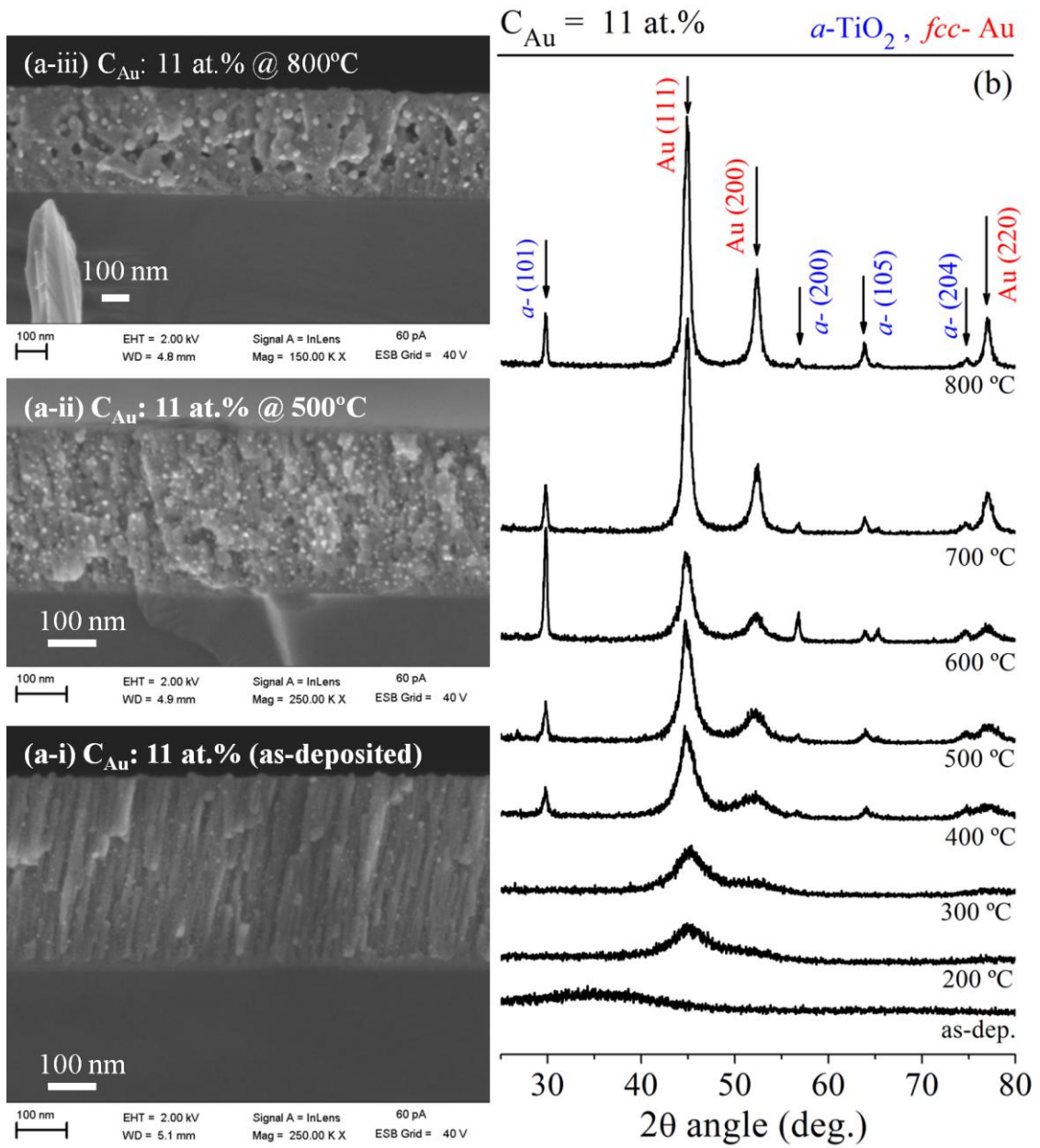**Figure 1**

Figure 2

Figure 3

Figure 4

Figure 5

Figure 6

(a) C_Au: 11 at.% (as-deposited)

20 nm

(b) C_Au: 11 at.% @300°C

20 nm

(c) C_Au: 11 at.% @ 600 °C

20 nm

(d) C_Au: 11 at.% @ 800 °C

50 nm

Figure 7

Figure 8

200 nm   EHT = 2.00 kV   Signal A = ESB   60 pA   N4#18_700
         WD = 4.8 mm   Mag = 150.00 K X ESB Grid = 1000 V
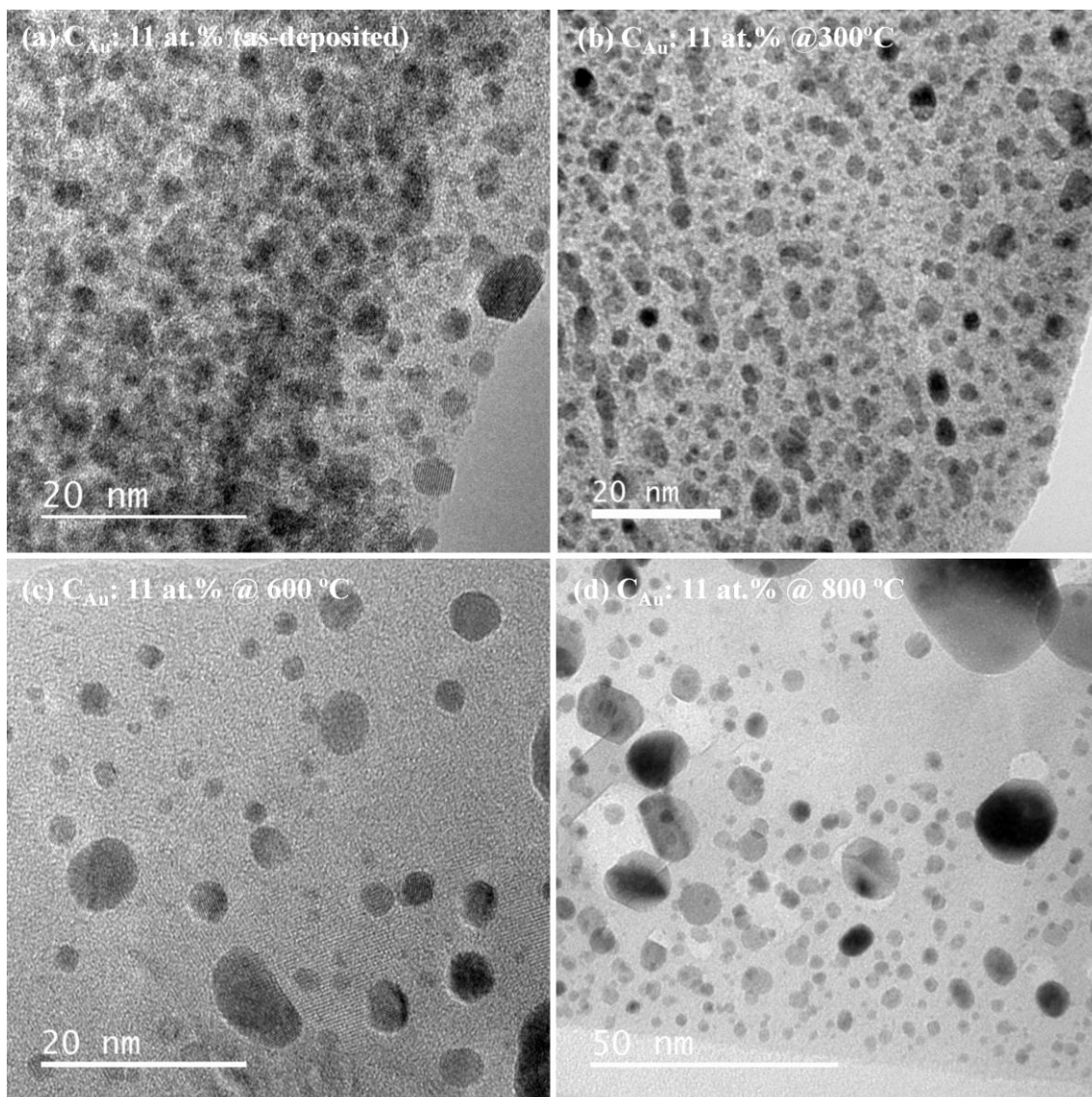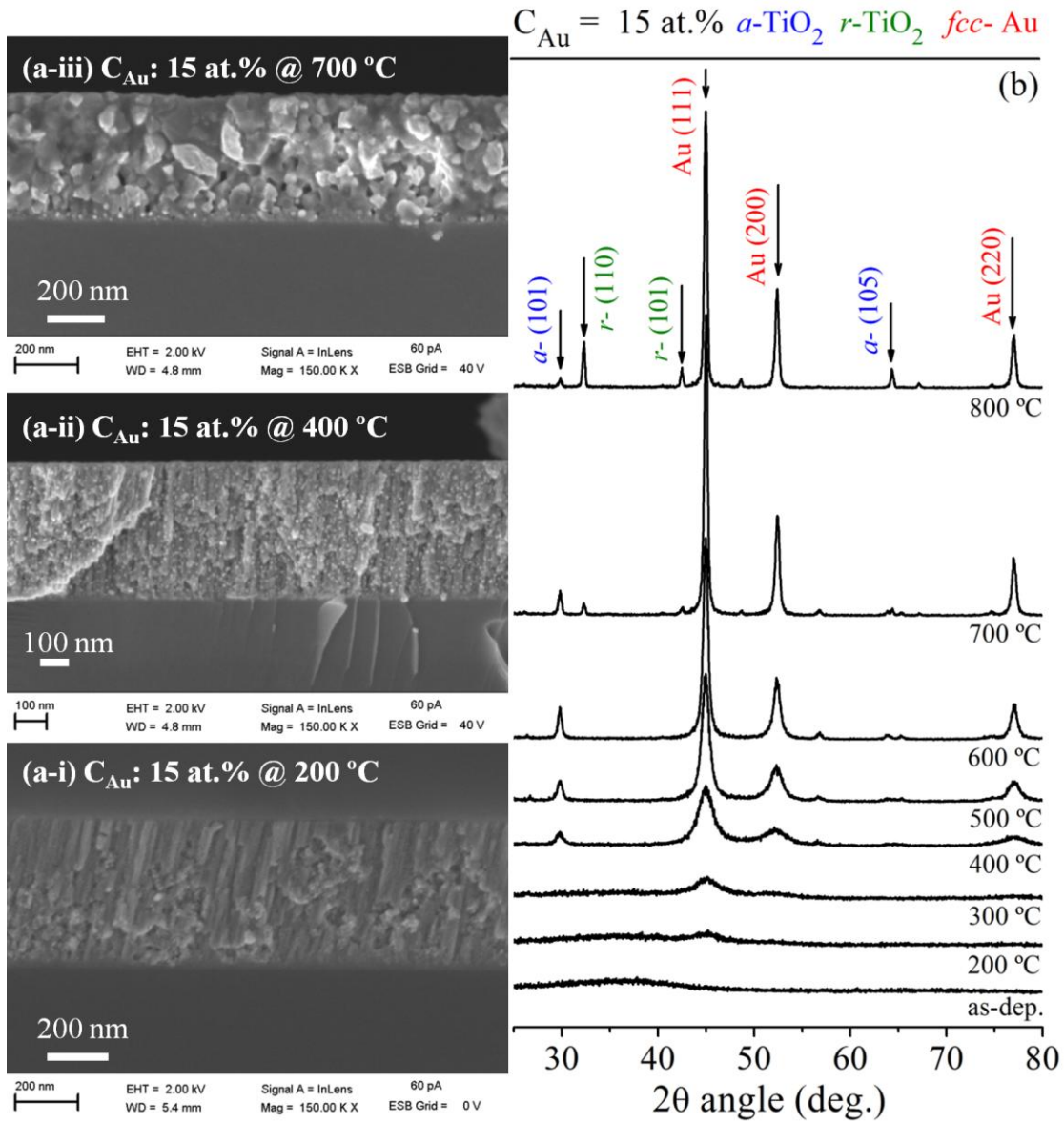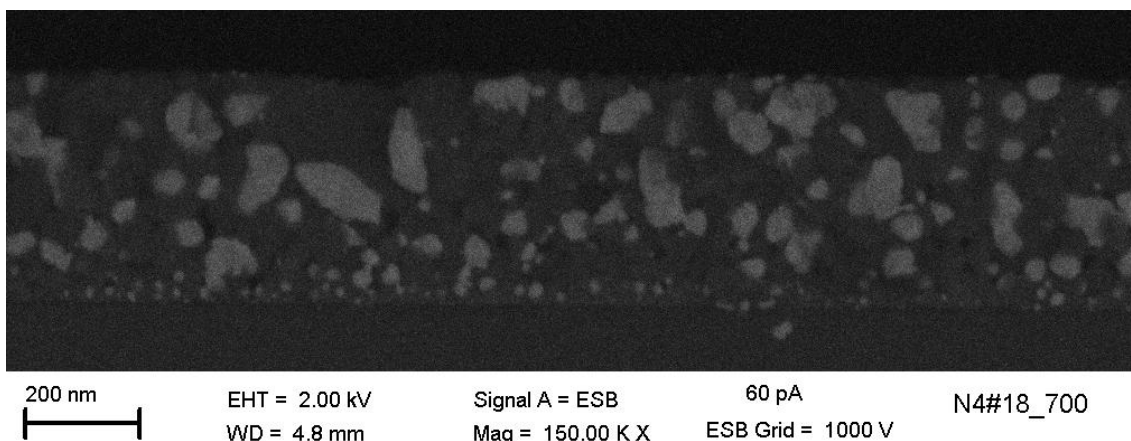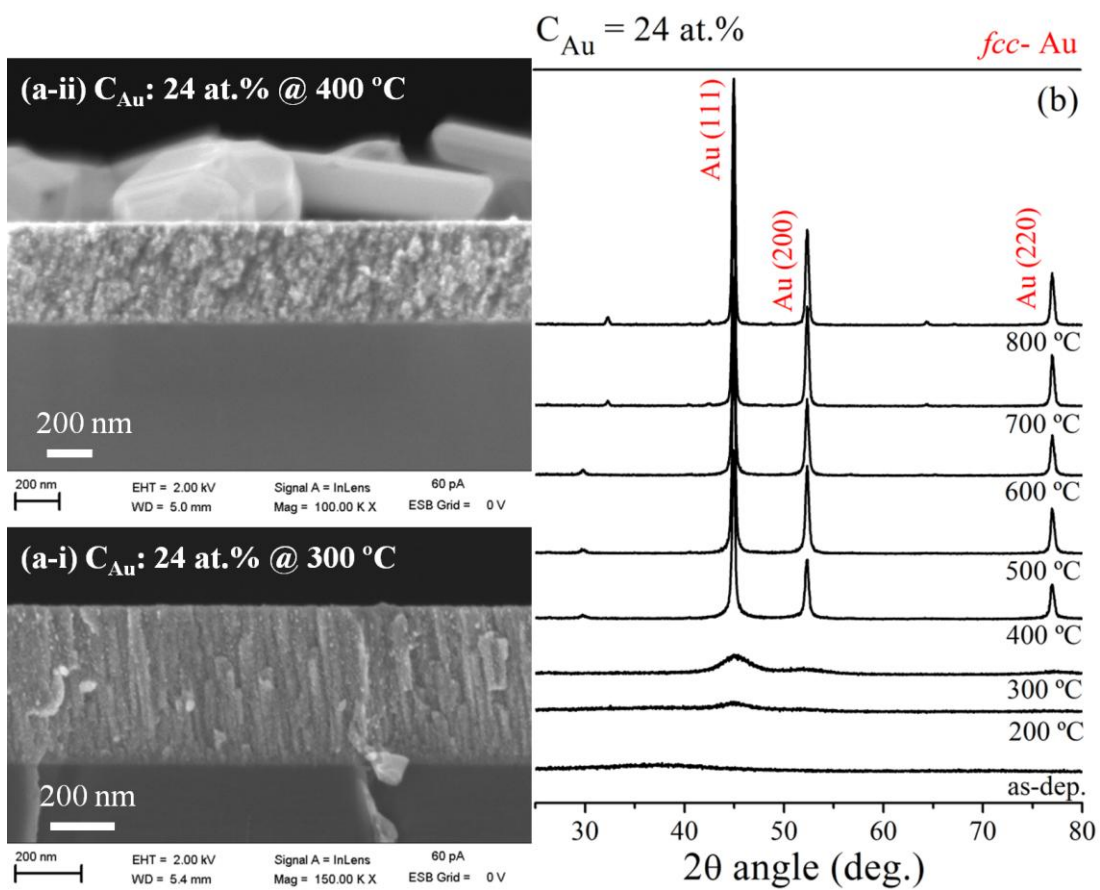
Figure 9

Figure 10

Figure 11

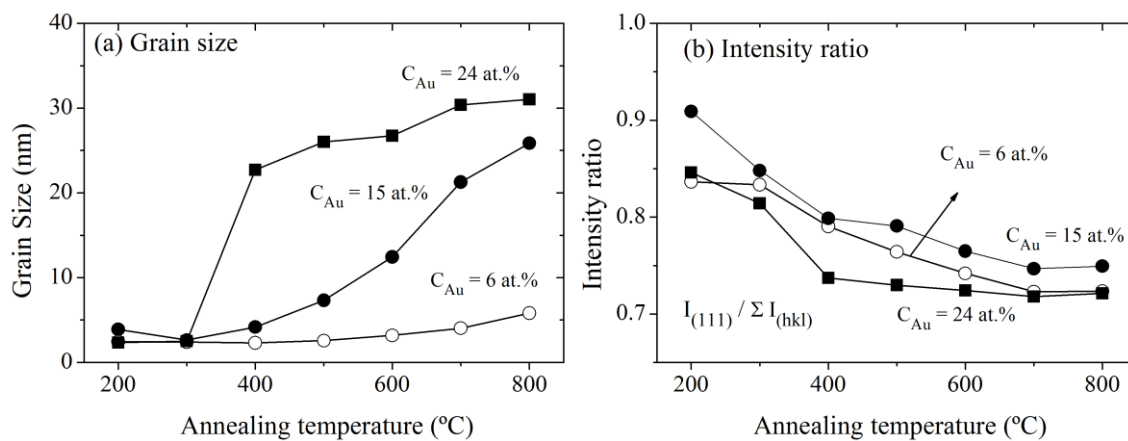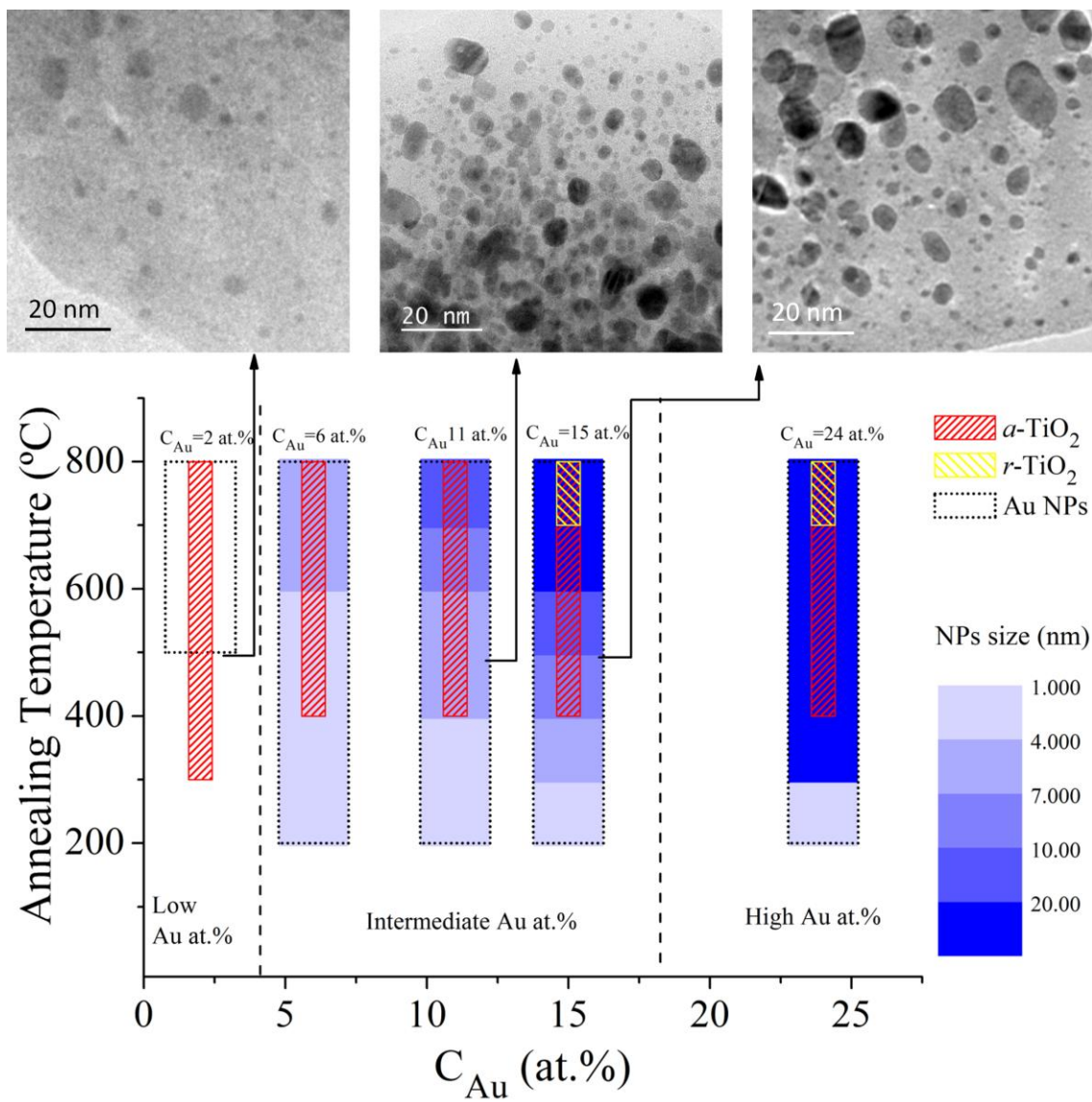**Figure 12**

Highlights

- Au:TiO$_2$ films were produced by magnetron sputtering and post-deposition annealing;
- The Au concentration in the films increases with the Au pellets area;
- Annealing induced microstructural changes in the films;
- The nanoparticles size evolution with temperature depends on the Au concentration

Highlights